Electronic Supplementary Material (ESI) for Journal of Materials Chemistry A.

Electronic Supplementary Information

Tailoring 2D MoS_2 heterointerfaces for promising oxygen reduction reaction electrocatalysis

Jianxin Mao, Peng Liu, Cuicui Du, Dongxue Liang, Jianyue Yan, Wenbo Song*

College of Chemistry, Jilin University, Changchun 130012, P.R. China.

**E-mail: wbsong@jlu.edu.cn; Fax: +86-431-85168420*

Contents:

1. Experimental details

Materials. Ammonium molybdate tetrahydrate, thiourea, melamine and nickel (II) chloride hexahydrate were purchased from Sinopharm Chemical Reagent. The Pt/C catalyst (20 wt% Pt on Vulcan XC72R carbon) was purchased from Johnson Matthey Corporation. Other chemicals were purchased from Beijing Chemical Reagent Company.

Synthesis of C_3N_4 template. Melamine is used as precursor for preparing C_3N_4, which is heated in a muffle furnace at 550 ℃ for 3 h with a programming rate of 4 ℃ min^{-1}. The yellow colored C_3N_4 powder is obtained after cooling to room temperature, and ready for further use.

Synthesis of ultrathin Ni_3S_2/MoS_2-0.2 nanosheets. 4.0 g of C_3N_4 intermediate, 2.0 g of thiourea, 0.16 g of ammonium molybdate tetrahydrate and 0.054 g of Nickel (II) chloride hexahydrate are mixed by grinding, and the mixture is firstly heated at 600 ℃ for 4 h with a programming rate of 2.5 ℃ min^{-1}. After that, the temperature was increased to 780 ℃ and maintained for another 5 h. The calcination is carried out in a nitrogen atmosphere. **HCN is formed in this step, please pay attention to tail gas treatment.**

Synthesis of ultrathin Ni_3S_2/MoS_2-0.05 nanosheets. The synthetic approach is similar to the ultrathin Ni_3S_2/MoS_2-0.2 nanosheets. The amount of Nickel (II) chloride hexahydrate is 0.014 g, the amount of ammonium molybdate tetrahydrate is 0.19 g.

Synthesis of ultrathin Ni_3S_2/MoS_2-0.1 nanosheets. The synthetic approach is similar to the ultrathin Ni_3S_2/MoS_2-0.2 nanosheets. The amount of Nickel (II) chloride hexahydrate is 0.027 g, the amount of ammonium molybdate tetrahydrate is 0.18 g.

Synthesis of ultrathin Ni_3S_2/MoS_2-0.15 nanosheets. The synthetic approach is similar to the ultrathin Ni_3S_2/MoS_2-0.2 nanosheets. The amount of Nickel (II) chloride hexahydrate is 0.041 g, the amount of ammonium molybdate tetrahydrate is 0.17 g.

Synthesis of ultrathin Ni_3S_2/MoS_2-0.3 nanosheets. The synthetic approach is similar to the ultrathin Ni_3S_2/MoS_2-0.2 nanosheets. The amount of Nickel (II) chloride hexahydrate is 0.081 g, the amount of ammonium molybdate tetrahydrate is 0.14 g.

Synthesis of ultrathin Ni_3S_2/MoS_2-0.4 nanosheets. The synthetic approach is similar to the ultrathin Ni_3S_2/MoS_2-0.2 nanosheets. The amount of Nickel (II) chloride hexahydrate is 0.108 g, the amount of ammonium molybdate tetrahydrate is 0.12 g.

Table S1. The content of raw materials for achieving different Ni_3S_2/MoS_2 samples.

sample name	**C_3N_4**	**thiourea**	**ammonium molybdate tetrahydrate**	**Nickel (II) chloride hexahydrate**
Ni_3S_2/MoS_2-0.05	4.0 g	2.0 g	0.19 g	0.014 g
Ni_3S_2/MoS_2-0.1	4.0 g	2.0 g	0.18 g	0.027 g
Ni_3S_2/MoS_2-0.15	4.0 g	2.0 g	0.17 g	0.041 g
Ni_3S_2/MoS_2-0.2	4.0 g	2.0 g	0.16 g	0.054 g
Ni_3S_2/MoS_2-0.3	4.0 g	2.0 g	0.14 g	0.081 g
Ni_3S_2/MoS_2-0.4	4.0 g	2.0 g	0.12 g	0.108 g

Synthesis of ultrathin MoS_2 nanosheets. 4.0 g of C_3N_4 intermediate, 2.0 g of thiourea and 0.2 g of ammonium molybdate tetrahydrate were mixed by grinding, and the resulting powder was transferred into the furnace. The furnace was heated to 600℃ at a rate of 2.5℃ min^{-1} under nitrogen and maintained for 240 min, followed by elevating the temperature to 780℃ and maintaining for 300 min.

Synthesis of ultrathin Ni_3S_2/MoS_2-0.2-700 nanosheets. 4.0 g of C_3N_4 intermediate, 2.0 g of thiourea, 0.16 g of ammonium molybdate tetrahydrate and 0.054 g of Nickel (II) chloride hexahydrate are mixed by grinding, and the mixture is firstly heated at 600 °C for 4 h with a programming rate of 2.5 °C min^{-1}. After that, the temperature was increased to 700 °C and kept for another 5 h. The calcination is carried out in a nitrogen atmosphere.

Synthesis of ultrathin Ni_3S_2/MoS_2-0.2-900 nanosheets. 4.0 g of C_3N_4 intermediate, 2.0 g of thiourea, 0.16 g of ammonium molybdate tetrahydrate and 0.054 g of Nickel (II) chloride hexahydrate are mixed by grinding, and the mixture is firstly heated at 600 °C for 4 h with a programming rate of 2.5 °C min^{-1}. After that, the temperature was increased to 900 °C and kept for another 5 h. The calcination is carried out in a nitrogen atmosphere.

2. Characterizations

Physical characterization. Scanning electron microscopy (SEM) measurements and energy dispersive X-ray (EDX) spectra were performed on a HITACHI SU8000 microscope. Transmission electron microscopy (TEM), high-resolution (HR)TEM and selected area electron diffraction (SAED) images were obtained on a JEOL JEM-2200FS microscope. The X-ray powder diffraction (XRD) patterns were measured in reflection mode (Cu Kα radiation) on a PANalytical B.V. Empyrean. X-ray Photoelectron Spectroscopy (XPS) spectra were recorded by using an ESCALAB 250 spectrometer with a monochromatic X-ray source with Al Kα excitation (1486.6 eV). Raman spectra were measured with a Horiba LabRAM HR Evolution spectrometer. Nitrogen sorption experiments were performed with a Quadrasorb-evo at 77K, and the sample was degassed at 150℃ for 20 h before measurements. The data were analysed with Quantachrome software.

Oxygen reduction reaction (ORR) measurements. The electrochemical tests were conducted using CHI 760e (Shanghai Chenhua Instrument Factory, China) with a typical three-electrode cell at 298 K. A platinum wire was used as the counter-electrode and a saturated calomel electrode (SCE) as the reference electrode. The working electrode was prepared by applying the catalyst turbid solution onto a pre-polished glassy carbon rotating disk electrode (RDE) (3 mm diameter). For each sample, 3 mg (20 wt% Pt/C is taken 1.5 mg) catalyst was dispersed in a mixed solvent of

0.5 mL ultrapure water and 0.5 mL DMF (volume ratio 1: 1). The mixture was ultrasonicated for 30~60 min to obtain the homogeneous dispersion. Then, 10 µL well-dispersed sample ink was dropped onto the glassy carbon electrode disk. The loading for each Ni_3S_2/MoS_2 sample and 20 wt% Pt/C catalyst was ~0.4 mg cm^{-2} and ~0.2 mg cm^{-2}, respectively. After drying at 298 K, 5 µL of 0.5 wt% Nafion solution in ethanol was dropped onto the surface of the catalyst layer to form a thin protective film. The addition of a little Nafion can effectively improve the distribution of the catalyst and enhance its binding onto the electrode surface. Before experiment, the electrolyte solutions were purged with O_2 for 30 min. The headspace of the electrochemical cell was continuously purged with O_2 during the electrochemical detection. All the experiments were conducted at ambient conditions. In this work, the onset potential is defined as the potential that the cathodic catalytic current exceeds 0.05 mA cm^{-2}. The Koutecky-Levich (K-L) plots were taking points at different electrode potentials. Based on the K-L equation, the electron transfer number (*n*) can be calculated from the slope of the K-L plot:

$$\frac{1}{J} = \frac{1}{J_K} + \frac{1}{B\omega^{1/2}} \qquad (1)$$

$$B = 0.62nFC_0(D_0)^{2/3}(v)^{-1/6} \qquad (2)$$

where J is the measured current density, J_k is the kinetic current density, ω is the rotation rate of the disk electrode, n is the number of electron transfers per O_2 molecule, F is the Faraday constant (96 485 C mol^{-1}), C_0 is the bulk oxygen concentration in 0.1 M KOH (1.2×10^{-6} mol cm^{-3}), D_0 is the oxygen diffusion coefficient in 0.1 M KOH (1.9×10^{-5} cm^2 s^{-1}), and v is the kinematic viscosity of the electrolyte (0.01 cm^2 s^{-1}).[1] All the potentials reported were referenced to a reversible hydrogen electrode (RHE).

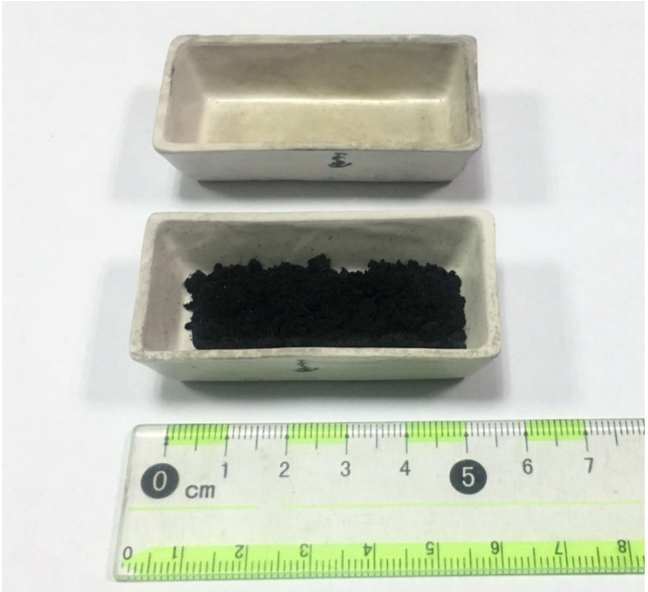

Fig. S1 Photograph of ultrathin Ni_3S_2/MoS_2 nanosheets (0.18 g).

Table S2. Elemental content in Ni_3S_2/MoS_2-0.2 and acid etched Ni_3S_2/MoS_2-0.2 by XPS analysis.

Sample	Chemical composition (at%)					
	S	Mo	C	N	O	Ni
Ni_3S_2/MoS_2-0.2	45.34	20.30	13.30	6.71	9.49	4.86
acid etched Ni_3S_2/MoS_2-0.2	56.16	24.21	6.56	0.87	5.96	6.24

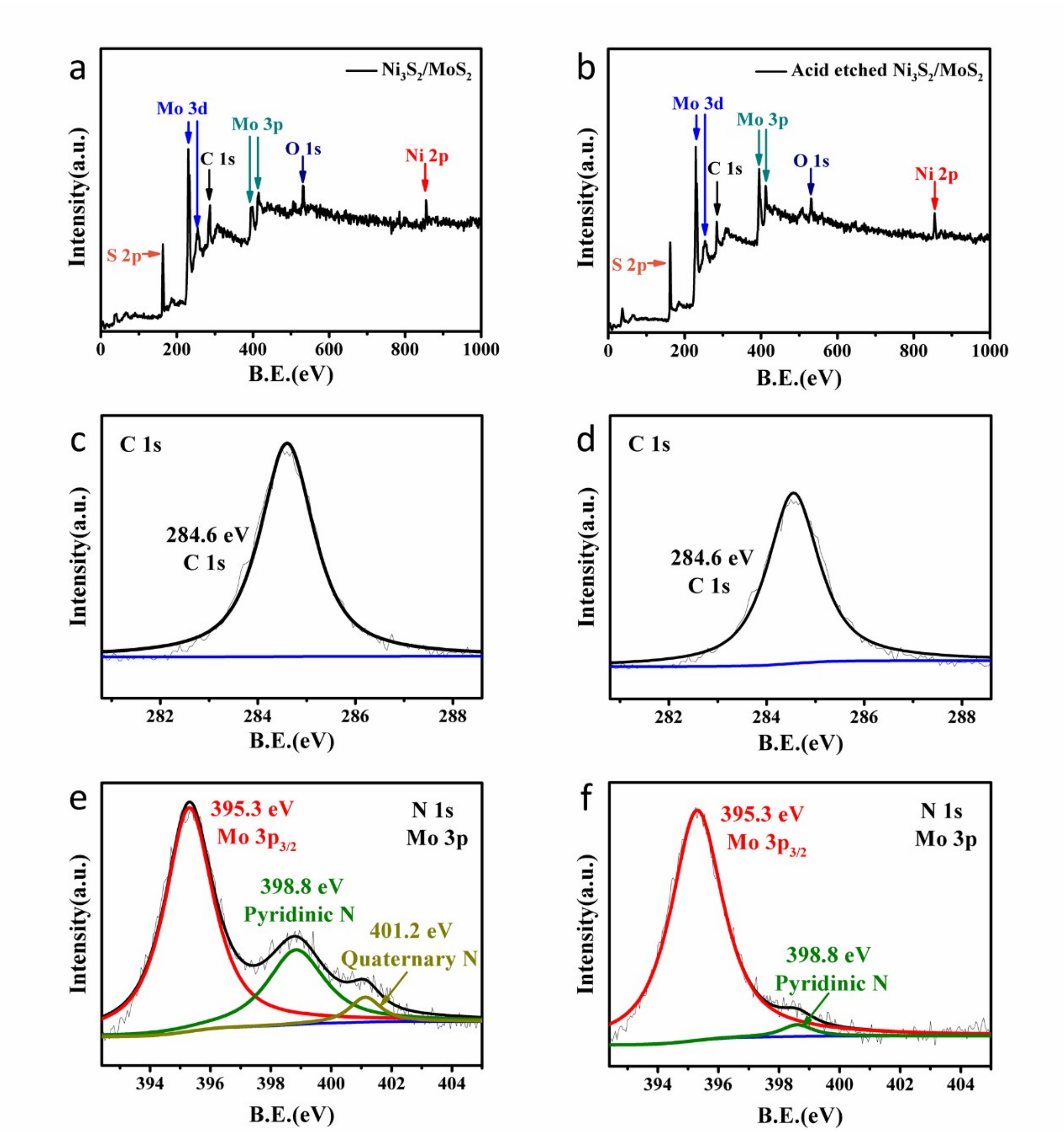

Fig. S2 XPS survey spectrum of Ni_3S_2/MoS_2 and acid etched Ni_3S_2/MoS_2-0.2.

The C and N may mainly originate from surface contamination. In literature, the 1s level hydrocarbon contaminant carbon is reported at 284.6 eV, which is in good agreement with the C 1s peak at 284.6 ± 0.2 eV in the XPS spectrum in Fig. S2a. The surface pollution to the sample is hard to avoid before XPS measurement. Meanwhile, the presence of the O 1s and N 1s peaks also evidence the surface pollution of the sample.

We have performed the acid etching experiment by dispersing 0.1 g Ni_3S_2/MoS_2-0.2 in 10 ml

1M HCl and stirring for 24 h at room temperature. The resulting solid was firstly filtrated and washed with abundant ultrapure water, and then dried at 60 ℃ overnight in vacuum drying oven.

The XPS survey spectrum of acid etched Ni_3S_2/MoS_2-0.2 is shown in Fig. S2b, and the element content determined by XPS is presented in Table S2. Obviously, both of the C and N content in the acid etching sample are greatly reduced, which corresponds to the surface pollution of the sample. Meanwhile, similar results are also found by comparing the high-resolution C 1s and N 1s XPS spectra of the freshly-prepared (Fig. S2c, e) and acid etching samples (Fig. S2d, f). The hydrochloric acid washing removed most of the surface C and N. In regards to the remaining C 1s signal at 284.6 eV in the acid etched Ni_3S_2/MoS_2-0.2, we have discussed with the specialized XPS scientist, who thinks it may be the carbon residual in the measuring apparatus. In conclusion, above acid etching results prove that at least most of the C and N comes from contamination.

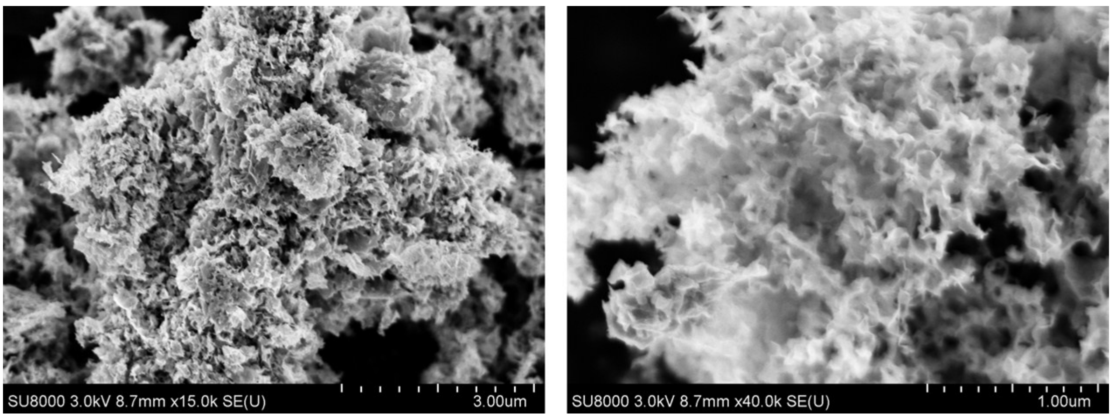

Fig. S3 SEM images at 15,000 times and 40000 times magnification of pristine MoS_2 ultrathin nanosheets.

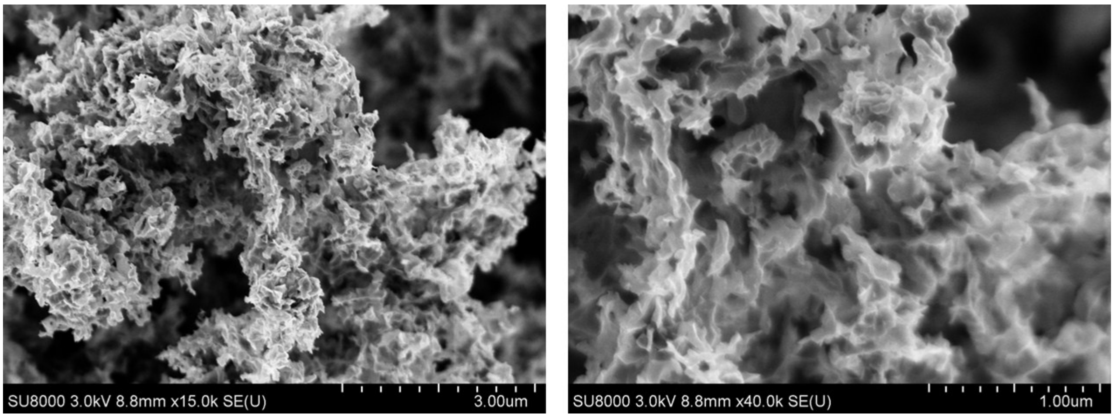

Fig. S4 SEM images at 15,000 times and 40000 times magnification of Ni_3S_2/MoS_2-0.05.

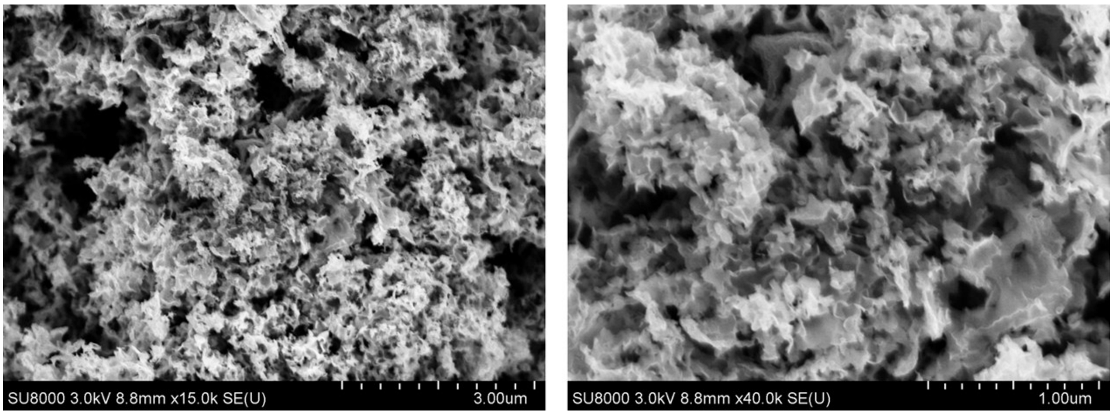

Fig. S5 SEM images at 15,000 times and 40000 times magnification of Ni_3S_2/MoS_2-0.1.

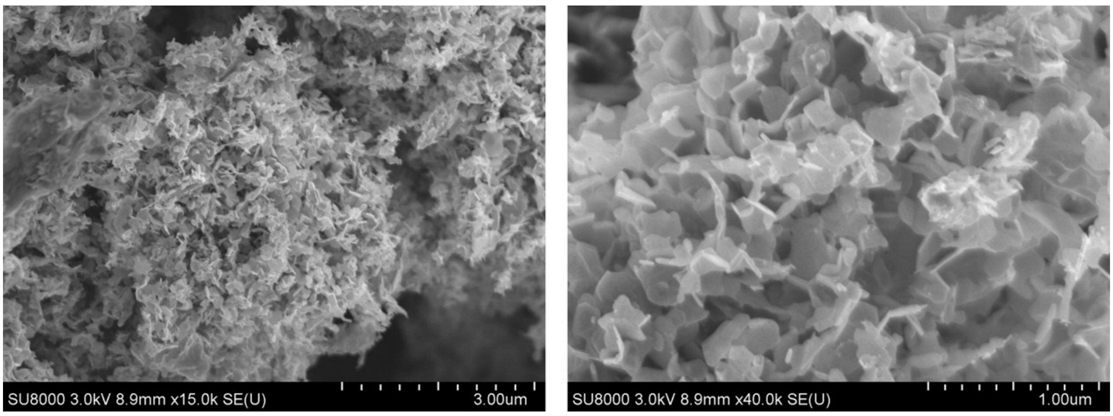

Fig. S6 SEM images at 15,000 times and 40000 times magnification of Ni_3S_2/MoS_2-0.15.

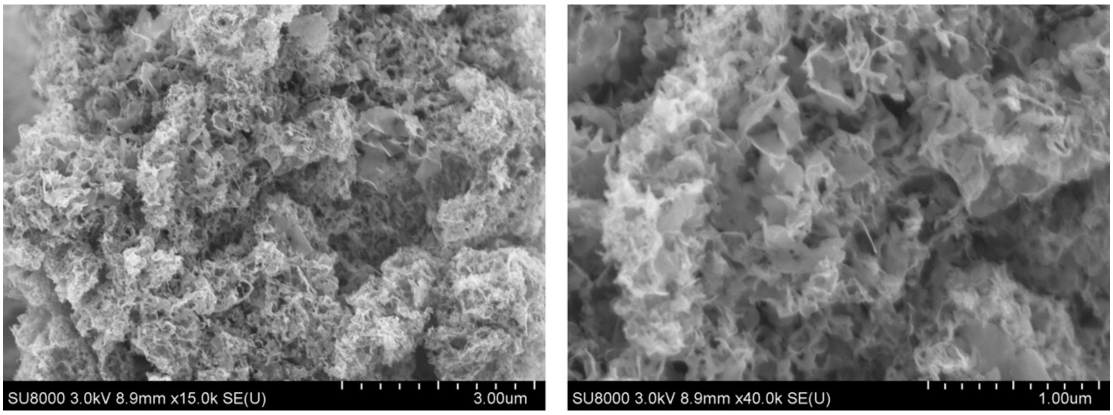

Fig. S7 SEM images at 15,000 times and 40000 times magnification of Ni_3S_2/MoS_2-0.2.

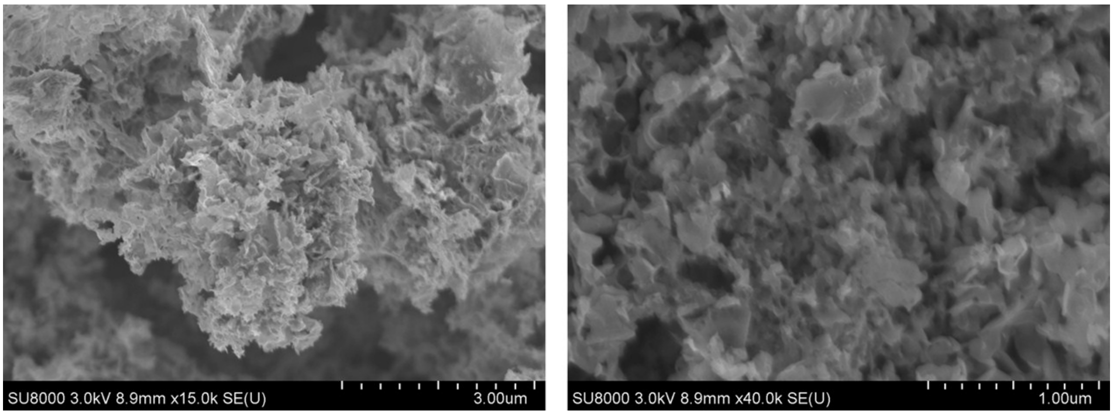

Fig. S8 SEM images at 15,000 times and 40000 times magnification of Ni_3S_2/MoS_2-0.3.

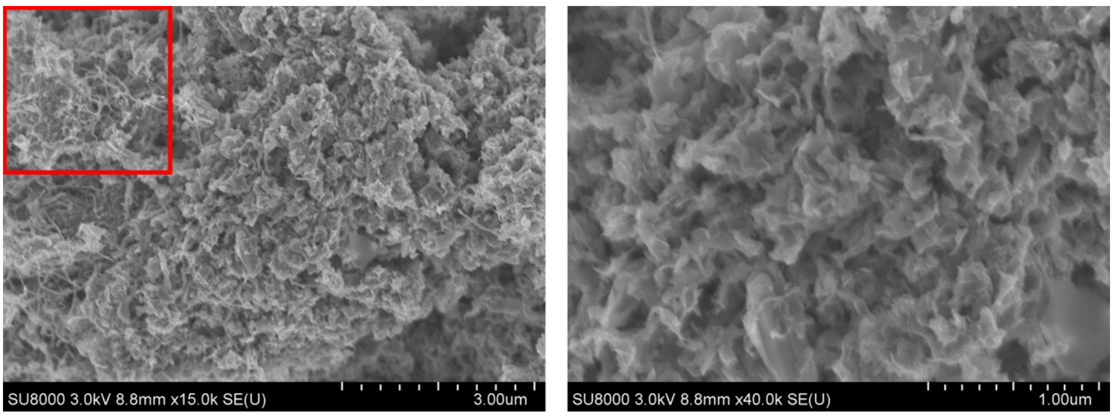

Fig. S9 SEM images at 15,000 times and 40000 times magnification of Ni_3S_2/MoS_2-0.4.

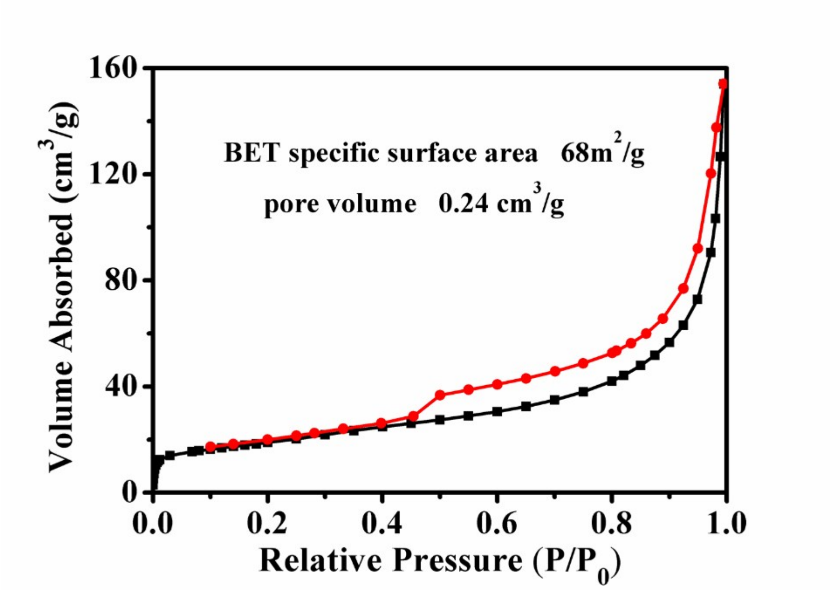

Fig. S10 Nitrogen sorption measurements for ultrathin Ni_3S_2/MoS_2 nanosheets.

The Brunauer-Emmett-Teller (BET) specific surface area of the Ni_3S_2/MoS_2 sample is investigated via nitrogen isothermal adsorption/desorption measurements. As shown in Fig. S10, the BET specific surface area is 68 m^2 g^{-1}, and the pore volume is 0.24 cm^3 g^{-1}. This is the type H3 hysteresis loops.[2] This character is associated with the metastability of the adsorbed multilayer (and delayed capillary condensation) and is due to the low degree of pore curvature and non-rigidity of the aggregate structure. It means that micrometer-sized 3D structure stacked by nanosheets is successfully produced.

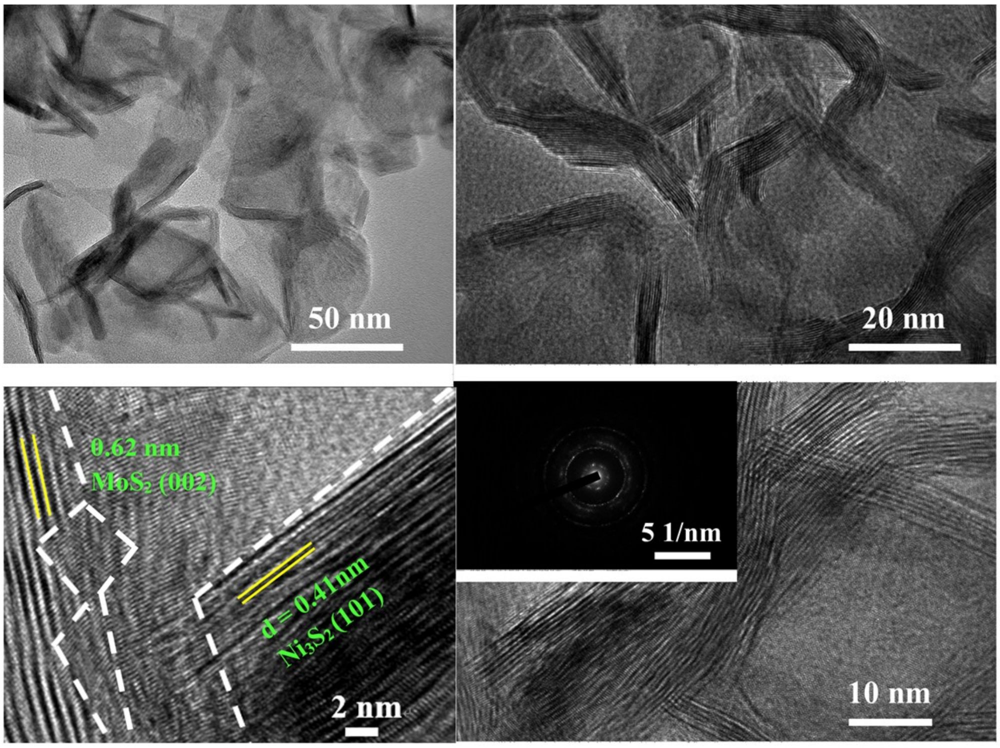

Fig. S11 TEM and HRTEM image of Ni_3S_2/MoS_2 ultrathin nanosheets (the image of SAED is inset in corresponding TEM image).

Selected area electron diffraction (SAED) of the sample is shown in the inset of Fig. S11. The different rings are composed of diffraction points. This result is in agreement with the crystal orientations of Ni_3S_2 and MoS_2. Since the luminance of the (002) planes of 2H-MoS_2 ring is weak, we know that the Ni_3S_2/MoS_2 nanosheets are ultrathin.

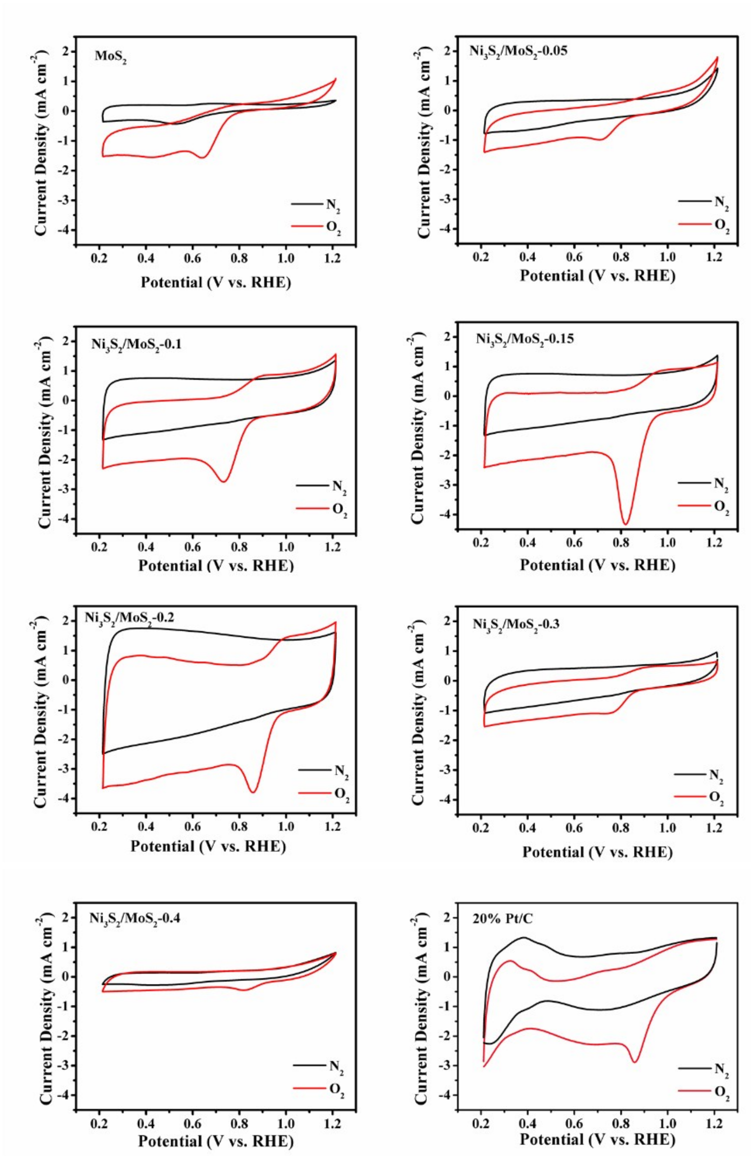

Fig. S12 CVs of various Ni_3S_2/MoS_2 samples, MoS_2 nanosheets and commercial Pt/C catalyst in N_2- (black) and O_2- (red) saturated electrolyte in 0.1M KOH with a scan rate of 50 mV s^{-1}.

The ORR activity of series of Ni_3S_2/MoS_2 samples are assessed by CV in O_2-saturated and N_2-saturated 0.1 M KOH electrolyte at a scan rate of 50 mV s^{-1}. As a control, the ORR performances of MoS_2 nanosheets and commercial Pt/C catalyst were also presented in Fig. S12. For samples Ni_3S_2/MoS_2-0.05, 0.1, 0.15 and 0.2, the onset and peak potentials shift towards the positive direction upon increasing the amount of Ni_3S_2. Meanwhile, the ORR current densities also increase gradually with increasing the amount of Ni_3S_2 between these 4 samples. The results presented above suggest that the heterointerfaces play a key role in ORR. However, the current densities of Ni_3S_2/MoS_2-0.2, 0.3 and 0.4 decrease with increasing the amount of Ni_3S_2. The high content of Ni_3S_2 may either be not sufficient for catalysis or delay charge transport among the conductive MoS_2 skeleton during the catalytic process.[3]

To get a rough insight into the correlation of nanotopography with ORR activity, the morphological evolution of the samples with tunable ratio of the two components is investigated (Fig. S3 ~ S9). Their ORR activity are also evaluated (Fig. 3a and Fig. S12). From these experimental data, we deduce that the 2D nanostructure damage in the sample would destroy the Ni_3S_2/MoS_2 heterointerface, leading to deterioration of the ORR performance. We also find that maintaining intact 2D nanostructure and providing rich heterointerfaces are vital to ORR activity proliferation. The advantages of Ni_3S_2/MoS_2 nanosheets include but not limited to these points. In summary, above morphological evolution study suggests that the heterointerface-related activity improvement is reasonable.

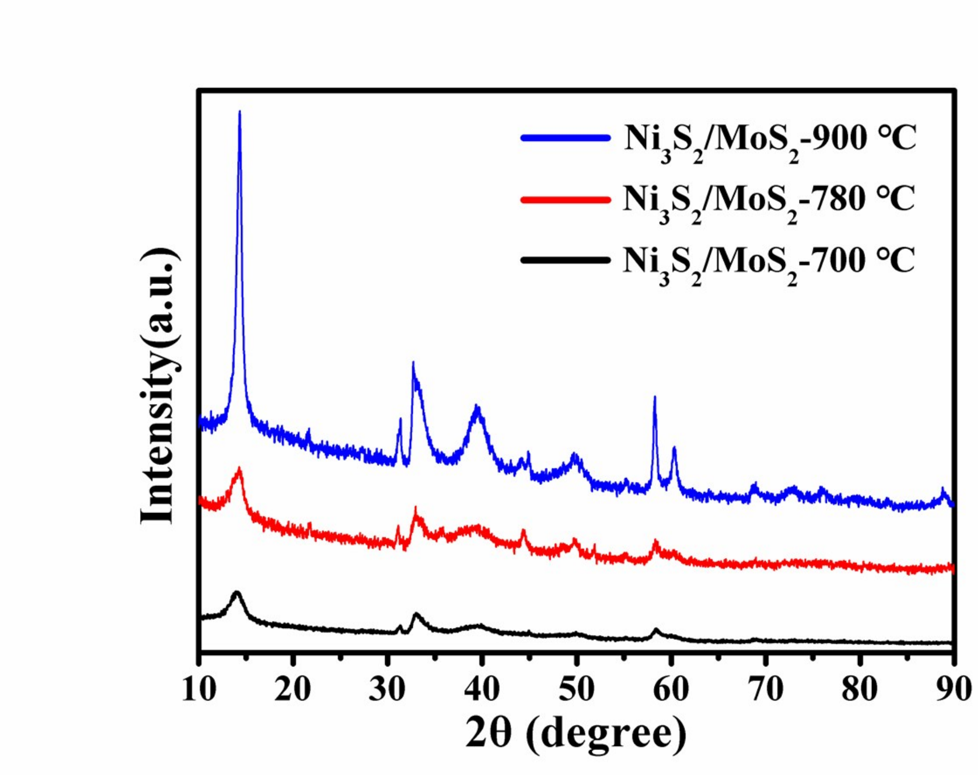

Fig. S13 XRD patterns of Ni_3S_2/MoS_2-0.2, Ni_3S_2/MoS_2-0.2-700 and Ni_3S_2/MoS_2-0.2-900.

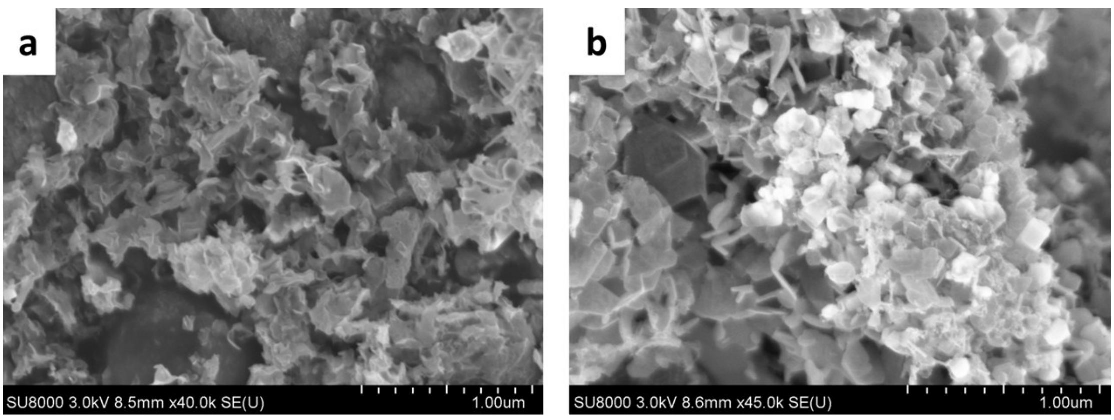

Fig. S14 SEM image of Ni_3S_2/MoS_2 ultrathin nanosheets. (a) Ni_3S_2/MoS_2-0.2-700. (b) Ni_3S_2/MoS_2-0.2-900.

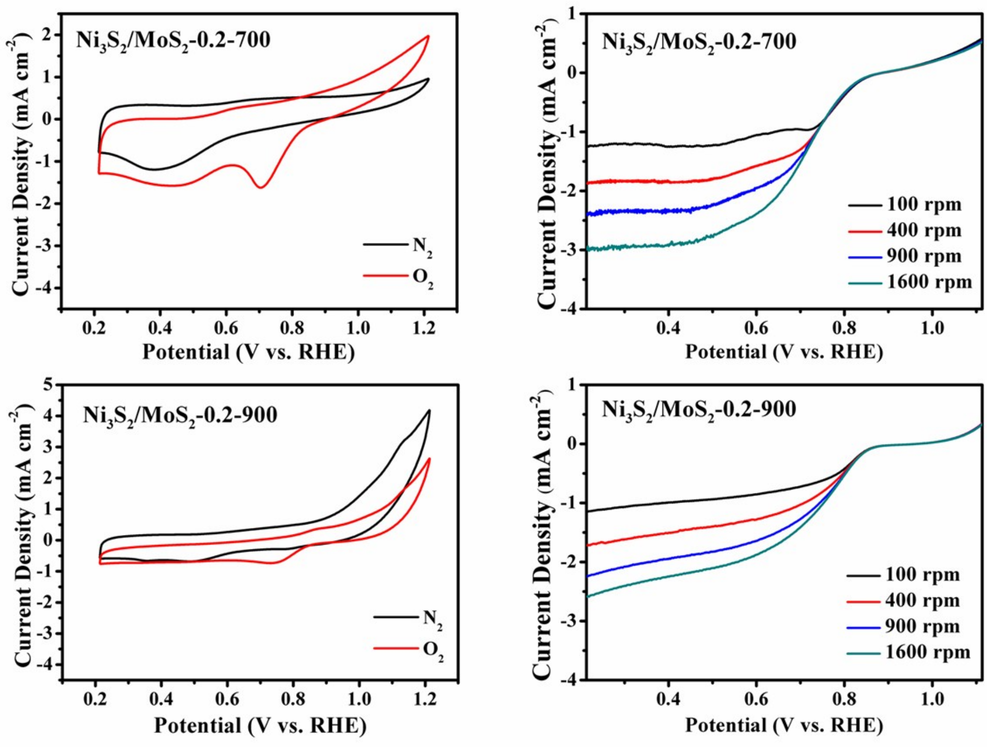

Fig. S15 CVs of Ni_3S_2/MoS_2-0.2-700 and Ni_3S_2/MoS_2-0.2-900 in N_2- (black) and O_2- (red) saturated electrolyte in 0.1M KOH with a scan rate of 50 mV s^{-1}, and LSVs of Ni_3S_2/MoS_2-0.2-700 and Ni_3S_2/MoS_2-0.2-900 (scan rate: 10 mV s^{-1}).

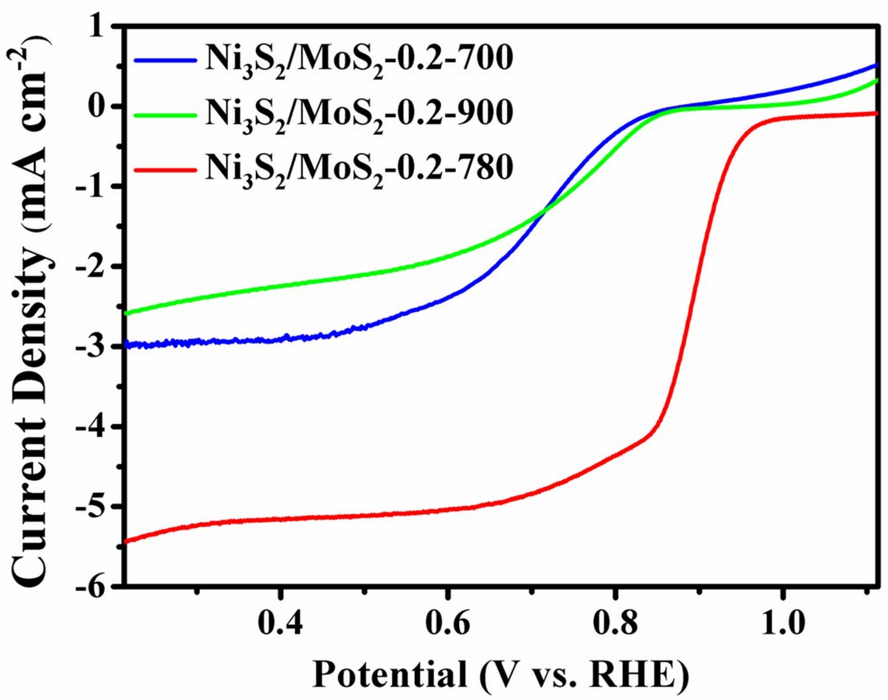

Fig. S16 LSVs of Ni_3S_2/MoS_2-0.2-700, Ni_3S_2/MoS_2-0.2 and Ni_3S_2/MoS_2-0.2-900 at 1600 rpm in O_2-saturated 0.1 M KOH (scan rate: 10 mV s^{-1}).

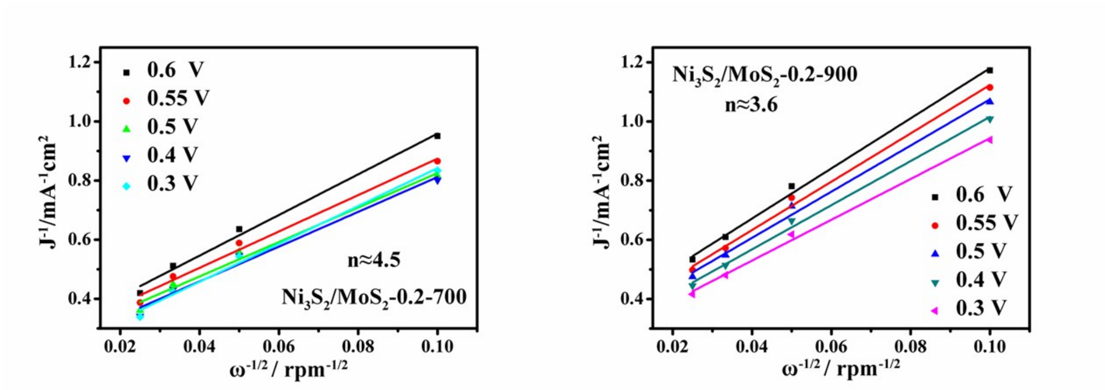

Fig. S17 The Koutecky–Levich plots of the Ni_3S_2/MoS_2-0.2-700 and Ni_3S_2/MoS_2-0.2-900.

The characterization and electrochemical results of the two samples synthesized at treating temperature of 700 ℃ and 900 ℃ are shown in Fig. S13~Fig.S17. One can see that as the pyrolysis temperature increases, the crystallinity of the materials increases significantly. The morphology of the two samples appears more irregular. When the pyrolysis temperature is 700 ℃, the low crystallinity causes an irregular nanostructure. When the heating temperature rises to 900 ℃, Ni_3S_2 melts at 797 ℃ and the nanostructures of the material is destroyed. The ORR performances of both samples are obviously much worse compared to Ni_3S_2/MoS_2-0.2. By analyzing the K-L plots in Fig. S17, the estimated electron transfer number of Ni_3S_2/MoS_2-0.2-700 and Ni_3S_2/MoS_2-0.2-900 is 4.5 and 3.6, respectively. The crystallinity of the former is low. The amorphous Ni_3S_2 and MoS_2 in alkaline solution are instable. It may cause side reactions on the working electrode during the ORR processes, so the electron transfer number is more than 4. While for the latter, since the pyrolysis temperature exceeds the melting point of Ni_3S_2, the Ni_3S_2 will melt and re-accumulate. The nanostructure and the heterointerfaces may thus be destroyed. This leads to deterioration of ORR performance and decrease in the electron transfer number.

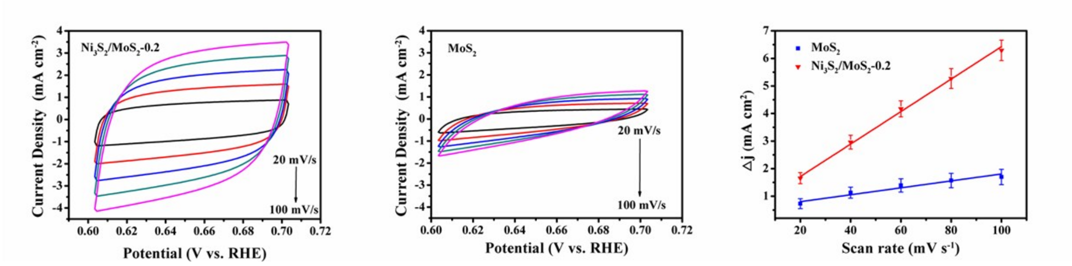

Fig. S18 CVs of Ni_3S_2/MoS_2 and MoS_2; Scan rate dependent-current densities at 0.66 V.

The amount of the catalytically active sites of Ni_3S_2/MoS_2-0.2 and MoS_2 nanosheets for ORR are estimated from the C_{dl} by collecting cyclic voltammograms in the non-Faradaic region (Fig. S18). The MoS_2 nanosheets exhibits a smaller C_{dl} value than that of Ni_3S_2/MoS_2-0.2, suggesting a higher ECSA for Ni_3S_2/MoS_2-0.2. As a consequence, the Ni_3S_2/MoS_2-0.2 catalyst possesses richer effective active sites for ORR.

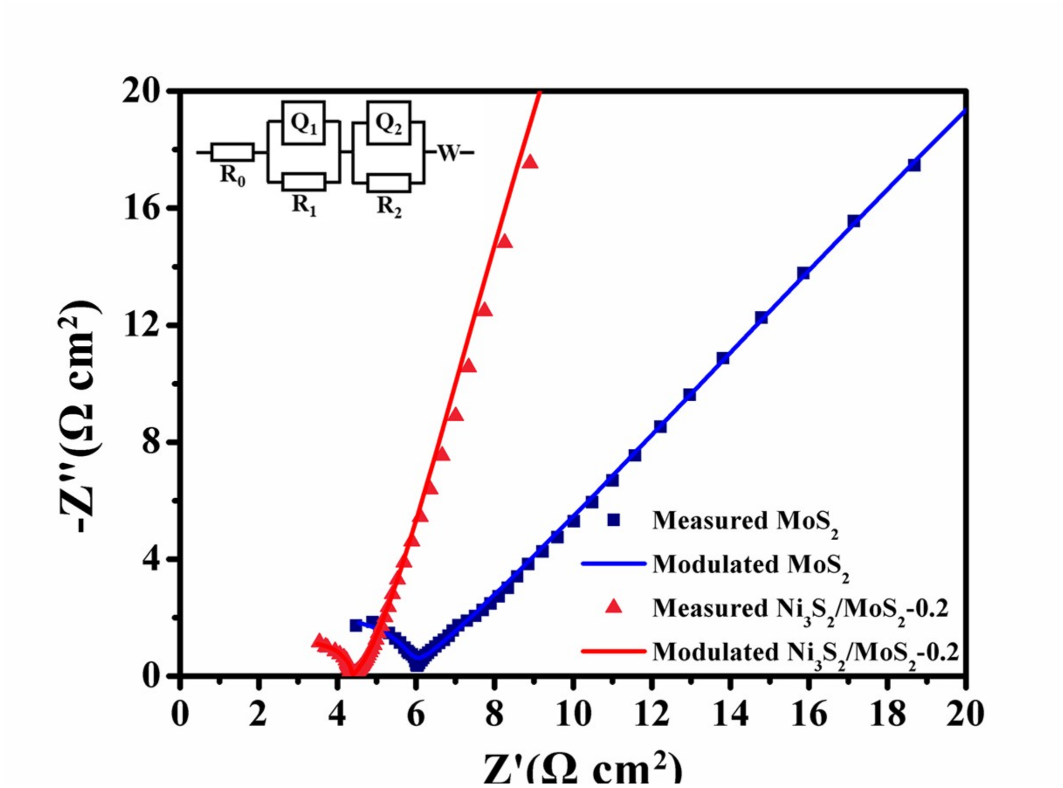

Fig. S19 Nyquist plots of Ni_3S_2/MoS_2 and MoS_2 in the frequency range of 1–1 M Hz, respectively; inset is the corresponding equivalent circuit.

Fig. S19 shows the electrochemical impedance spectroscopy (EIS) tests of the Ni_3S_2/MoS_2 catalyst and MoS_2 nanosheets. It was shown that the modulated results suited well with the tested results. R0 (29.31 Ω) is the Ohmic resistance that is originated from the contact resistance of the catalyst with the electrode surface. R1 and R2 were oxygen reduction reaction resistances.

The values of R1 and R2 were 32.36 Ω and 5627 Ω. It is usually believed that the oxygen reduction involves 4-electron and 2-electron reactions. The oxygen molecular was directly transformed into hydroxide ion in 4-electron reaction style and the intermediate of H_2O_2 was produced in the 2-electron reaction process and then transformed into hydroxide ion in the ORR reaction in alkaline electrolyte. The R1 corresponds to the mixed reaction of 4-electron and the first step of 2-elelectron ORR. Thus, the R2 corresponds to the second step of 2-electron ORR.

The value of R1 was much lower than that of R2, based on which it could be deduced that the intermediate H_2O_2 should be in a low concentration.[4] Considering the aforementioned results from Fig. S12 and Fig. S19, the catalytic process is mainly happened at the heterointerfaces, along which the embedded Ni-S sites and Mo edges chemisorb oxygen, and the Mo edges on 2D-MoS_2 display a four-electron process with the main product of hydroxide that is similar to the commercial Pt/C catalyst.

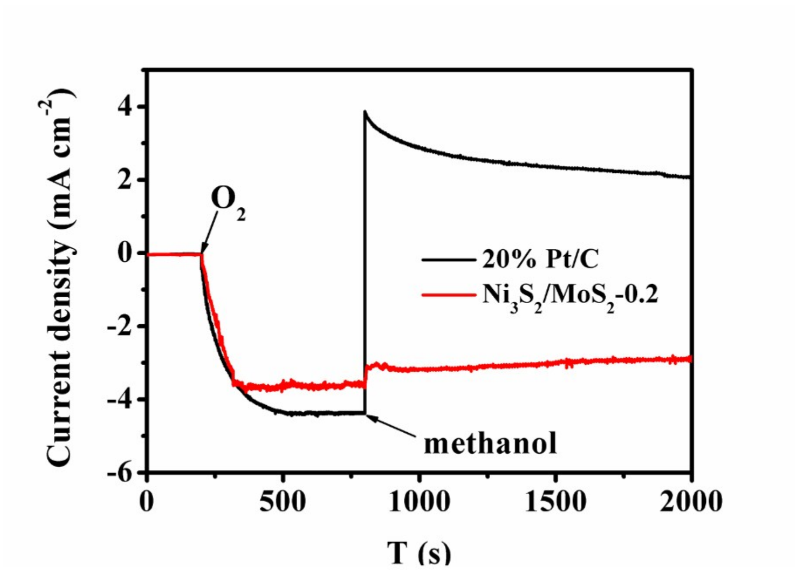

Fig. S20 Chronoamperometric response of Ni_3S_2/MoS_2 and 20% Pt/C catalyst (the arrow indicates introduction of 10 vol% methanol).

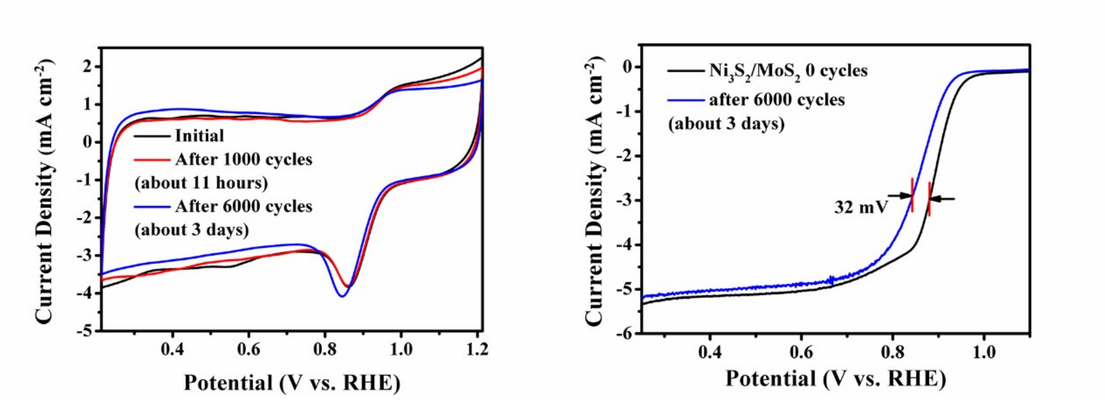

Fig. S21 Stability of Ni_3S_2/MoS_2 catalyst by comparing the CV measurements of the initial sample and after 1000/6000 consecutive cycles in 0.1 M KOH solution with a scan rate of 50 mV s^{-1} and LSV measurements at 1600 rpm with a scan rate of 10 mV s^{-1} of the initial sample and after 6000 consecutive cycles (0.21 V-1.21 V, CV, 50 mV s^{-1}) in 0.1M KOH solution.

Table S3. ORR performance comparison under alkaline conditions for Ni_3S_2/MoS_2 and related MoS_2-based materials.

Catalyst	Onset Potential (V vs. RHE)	$E_{1/2}$ (V vs. RHE)	Current density (mA cm^{-2}) @E/V (vs RHE)	Electron transfer number @E/V (vs RHE)	Refs.
Ni_3S_2/MoS_2 nanosheets	**0.950**	**0.885**	**5.16@0.4**	**4.01@0.8**	**This work**
MoS_2-CNT	about 0.75	about 0.65	about 5.6@0.264	about 4.2@0.6	5

P-MoS_2	0.96	0.80	about 3.3@0.4	3.6@0.8	6
MoS_2-Co-C	about 0.9	0.82	about 4.7@0.364	about 4	7
MoS_2-coupled polymer	about 0.9	0.824	4.9@0.064	3.7@0.564	8
AuNP–MoS_2 films	0.909	about 0.8	3.9@0.4	2.1-2.2	9
Flower-like MoS_2	0.824	about 0.7	2.4@0.164	3-3.4	10
MoS_2-RGO	0.8	about 0.7	2.72@0.3	3@0.5	11
O-MoS_2	0.94	0.80	3.8@0.3	4.1@0.8	12
MoS_2/NG	0.889	about 0.7	3.9@0.2	3.75-3.90	13
MoS_2QDs@Ti_3C_2TxQDs @MMWCNTs	0.87	0.75	3.9@0.4	3.95	14
CoO_x/mC@MoS_2@g-C_3N_4	0.89	about 0.7	4.4@0.4	3.6@0.3	15
N-GQDs/MoS_2–rGO	0.81	about 0.6	2.56@0	3.2-2.8	16
G@N-MoS_2	0.82	about 0.7	4.8@0	--	17
Mo–N/C@MoS_2	0.90	0.81	5.1@0.4	about 3.96	18

RHE potentials conversion from the original potentials in the reference.

E (vs. RHE) =E (vs. Hg/HgO) + 0.0591pH + 0.098,

E (vs. RHE) = E (vs. Ag/AgCl) + 0.0591pH + 0.197,

E (vs. RHE) = E (vs. SCE) + 0.0591pH + 0.242,

E (vs. RHE) = E (vs. NHE) + 0.0591pH.

Reference:

1. S. Inamdar, H.-S. Choi, P. Wang, M. Y. Song and J.-S. Yu, *Electrochem. Commun.*, 2013, **30**, 9-12.
2. K. S. Sing and R. T. Williams, *Adsorption Science & Technology*, 2004, **22**, 773-782.
3. C. Du, H. Huang, X. Feng, S. Wu and W. Song, *J. Mater. Chem. A*, 2015, **3**, 7616-7622.
4. T. Huang, H. Fang, S. Mao, J. Yu and L. Qi, *Carbon*, 2018, **126**, 566-573.
5. C. Lee, S. Ozden, C. S. Tewari, O. K. Park, R. Vajtai, K. Chatterjee and P. M. Ajayan, *ChemSusChem*, 2018, DOI: 10.1002/cssc.201800982.
6. H. Huang, X. Feng, C. Du and W. Song, *Chem Commun (Camb)*, 2015, **51**, 7903-7906.
7. K. Yuan, X. Zhuang, T. Hu, L. Shi, S. Sfaelou, U. Polnick, M. Forster, T. Pichler, T. Riedl, X. Feng, Y. Chen and U. Scherf, *ChemElectroChem*, 2017, **4**, 709-715.
8. K. Yuan, X. Zhuang, H. Fu, G. Brunklaus, M. Forster, Y. Chen, X. Feng and U. Scherf, *Angew Chem Int Ed Engl*, 2016, **55**, 6858-6863.
9. T. Wang, J. Zhuo, Y. Chen, K. Du, P. Papakonstantinou, Z. Zhu, Y. Shao and M. Li, *ChemCatChem*, 2014, **6**, 1877-1881.
10. C. Suresh, S. Mutyala and J. Mathiyarasu, *Mater. Lett.*, 2016, **164**, 417-420.
11. J. Zhou, H. Xiao, B. Zhou, F. Huang, S. Zhou, W. Xiao and D. Wang, *Appl. Surf. Sci.*, 2015, **358**, 152-158.
12. H. Huang, X. Feng, C. Du, S. Wu and W. Song, *J. Mater. Chem. A*, 2015, **3**, 16050-16056.
13. K. Zhao, W. Gu, L. Zhao, C. Zhang, W. Peng and Y. Xian, *Electrochim. Acta*, 2015, **169**, 142-149.
14. X. Yang, Q. Jia, F. Duan, B. Hu, M. Wang, L. He, Y. Song and Z. Zhang, *Appl. Surf. Sci.*, 2019, **464**, 78-87.
15. L. He, B. Cui, J. Liu, M. Wang, Z. Zhang and H. Zhang, *ACS Sustainable Chem. Eng.*, 2018, **6**, 9257-9268.
16. R. Vinoth, I. M. Patil, A. Pandikumar, B. A. Kakade, N. M. Huang, D. D. Dionysios and B. Neppolian, *ACS Omega*, 2016, **1**, 971-980.
17. C. Tang, L. Zhong, B. Zhang, H.-F. Wang and Q. Zhang, *Adv. Mater.*, 2018, **30**, 1705110.
18. I. S. Amiinu, Z. Pu, X. Liu, K. A. Owusu, H. G. R. Monestel, F. O. Boakye, H. Zhang and S. Mu, *Adv. Funct. Mater.*, 2017, **27**, 1702300.